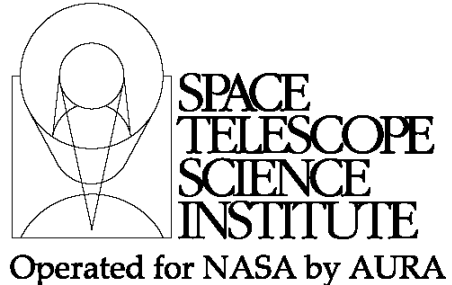# TECHNICAL REPORT

Operated for NASA by AURA

Title: Improved PSF Simulations for James Webb: Methods, Algorithms, and Validation	Doc #: JWST-STScI-002469, SM-12 Date: August 3, 2011 Rev: -
Authors: Marshall Perrin Phone: 410-338-4789	Release Date: 28 September 2011

1.0 Summary

This document describes a new software package for producing simulated PSFs for JWST. This package, WebbPSF, supercedes and replaces the existing JWPSF package to add a substantial amount of new functionality. In particular, it supports all instruments on JWST (including TFI and FGS, which JWPSF lacked), adds support for all the coronagraphic modes and TFI NRM, and has improved fidelity to instrumental properties. A detailed list of enhancements is included below. In addition to these external improvements visible to users, WebbPSF's internals include more sophisticated algorithms for optical propagation, and realistic treatment of broadband PSFs using synthetic photometry with measured instrument throughputs consistent with the preliminary JWST Exposure Time Calculators.

This document describes the motivation for creating WebbPSF, provides examples demonstrating its use, and discusses the algorithms and data used therein. The associated software manual, available on the web, provides more extensive descriptions of individual software functions and detailed calling conventions. To motivate certain default settings used with WebbPSF, I analyze the necessary sampling in wavelengths and detector subpixels needed to achieve a desired level of numerical fidelity in simulated PSFs. Finally, I present a large suite of verification tests that demonstrate WebbPSF produces results consistent with other simulation tools and our expectations for JWST.

2.0 Introduction

Good imaging performance is key to enabling the planned science program with JWST. Requirements on image quality derived from the science case have been used throughout mission development to guide the design of the observatory and instruments. Being able to perform the inverse transformation (i.e., turning designed or as-built observatory properties into simulated PSFs) is important now for enabling us to assess the current design and plan operations, and will be even more important during the mission for providing detailed PSF knowledge for data analysis and calibration. The Tiny Tim PSF

simulator for Hubble (Krist 1995; Hook & Stoehr 2008) has ably demonstrated the value of PSF simulations for observation planning, modeling, and analysis tasks such as deconvolution and PSF subtraction. Our ability to model HST PSFs has dramatically improved over time (e.g. Makidon et al. 2006; Anderson and King 2006). A similar capability will surely be needed for JWST.

To meet this need, already a variety of optical models have been developed, most notably JWPSF (Cox & Hodge 2006). Summaries of modeling tools available at STScI are provided by Makidon et al. (2007) and Soummer (2010).

WebbPSF is a new software package that computes simulated PSFs for the JWST instruments, taking into account updated OTE wavefront error models, instrumental properties such as detector pixel scales, rotations, and filter profiles, and input point source spectra. It replaces JWPSF to provide support for the entire suite of JWST instruments with improved calculation algorithms as detailed below.

WebbPSF is *not* a full optical model of JWST, but rather a tool for transforming optical path difference (OPD) maps, created with some other tool, into the resulting PSFs as observed with JWST's instruments. At present, such OPDs may be generated using Ball Aerospace's Integrated Telescope Model (ITM) or IPAM programs, or directly from the Code V segmented telescope model. Ultimately, we will generate OPDs for each instrument as a function of field position and time based on WFS&C data, using software packages still to be developed.
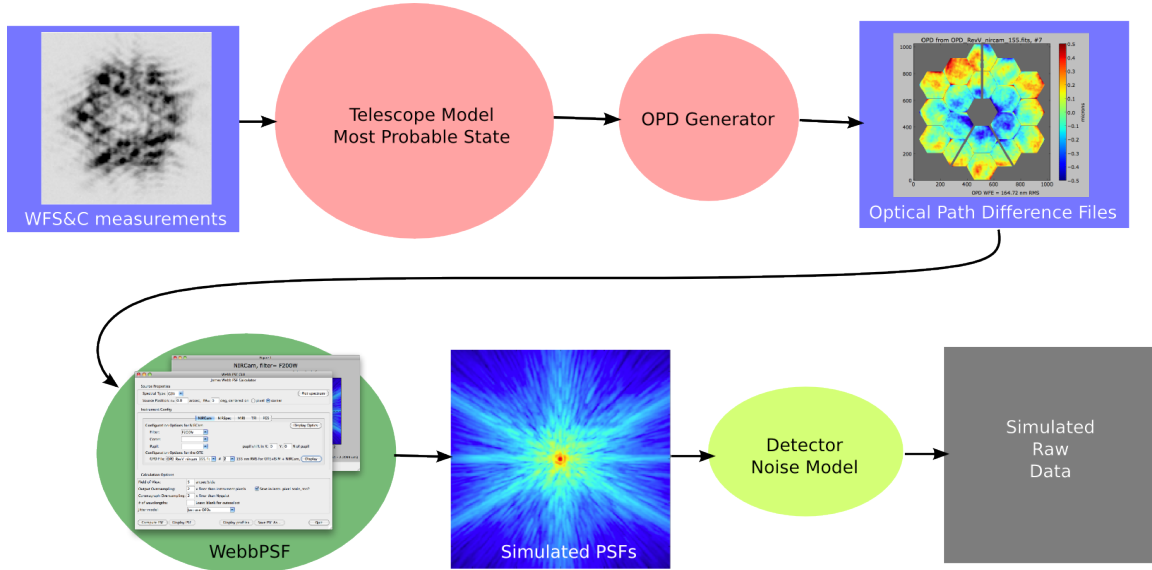

Figure 1: Eventual data flow for JWST simulations. The components marked in red are yet to be developed. Good detector models already exist but are not yet integrated with WebbPSF.

Check with the JWST SOCCER Database at: http://soccer.stsci.edu/DmsProdAgile/PLMServlet

To verify that this is the current version.

2.1 Why a new JWST PSF simulator?

Given that the JWPSF package has been available for several years now, one might ask why do we need a new PSF simulator? From a user's perspective this new code provides the following enhancements:

- Uses the most recent JWST pupil and OPD models, Revision V.
- Adds support for TFI and FGS.
- Updates filter lists for each instrument, and adds measured filter and instrument throughputs where available.
- Adds support for coronagraphic observations with MIRI, NIRCam, and TFI, and TFI non-redundant aperture masking (NRM). Note that MIRI coronagraphy models were already available using the JWcorPSF code split from JWPSF, but with substantial limitations on computation such as a fixed oversampling factor. NIRCam and TFI coronagraphy were not supported at all prior to now in models available at the S&OC.
- Includes the detector rotations, particularly for MIRI and NIRSpec
- Adds ability to arbitrarily adjust output image FOV size and pixel sampling separate from the oversampling factor used for the optical propagation.
- Many minor updates to instrument properties, such as proper pixel scales for NIRCam SW and LW channels and field rotations for MIRI and NIRSpec.
- New & improved graphical user interface.

Perhaps even more importantly, the underlying codebase has been entirely replaced and revamped. The most significant additions from a programmer's perspective include:

- Much cleaner object-oriented interface, with better abstraction of details across layers.
- Support for optics defined by analytic functions in addition to FITS images.
- Support for coordinate rotations and rotated optics.
- Arbitrary oversampling for coronagraphic models.
- Quick calculations using optimized matrix Fourier transforms and the fast semi-analytic coronagraphic propagation algorithms from Soummer et al. 2007.
- Uses the FFTW3 library for improved speed and efficient use of multiple processor cores.
- Uses the pysynphot library (same as the HST & Webb exposure time calculators) for consistent treatment of filter bandpasses and source spectra.

2.2 Obtaining and Using the Software

WebbPSF is written in Python and should run on any platform that supports the standard numpy/scipi/matplotlib packages. Download and installation instructions are available at http://www.stsci.edu/jwst/software/webbpsf. It depends on several standard modules for

scientific computing in Python: numpy, scipy, matplotlib, pyfits, atpy. The pysynphot module is optional but highly recommended as it improves the fidelity of broadband PSF calculations, while the FFTW3 module is optional but recommended for improved speed.

A graphical user interface is provided for interactive use, but it is expected that many uses will involve scripting, and the software interface has been designed with this in mind. Example code demonstrating all functionality is available in the software manual. In addition to its primary task of computing PSFs, WebbPSF also includes a suite of functions for measuring PSF properties such as FWHM, encircled energy, and Strehl ratio, and for displaying and plotting PSFs and derived quantities.
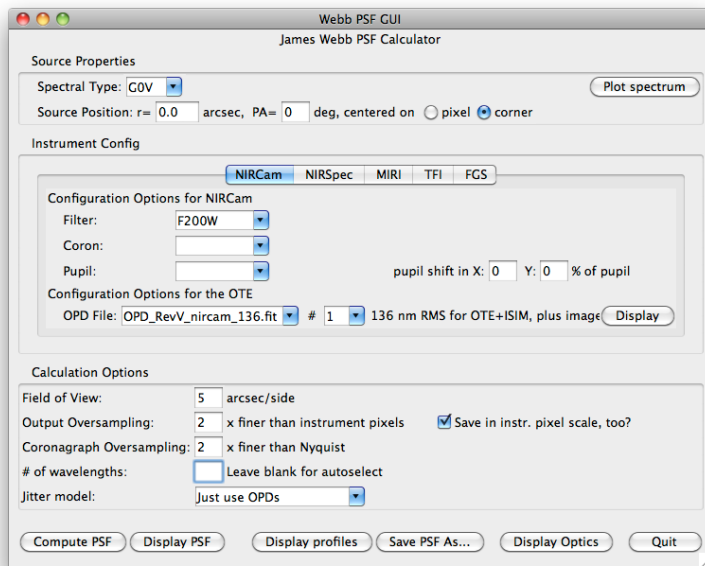

Figure 2: The WebbPSF graphical user interface. From top to bottom, sections allow control of source properties, instrument configuration, and options for the PSF calculation algorithm.

3.0 Examples

We show here just a few example results demonstrating the functionality of WebbPSF. More extensive analyses of PSF properties are given in section 6.0 below.

NIRCam, filter= F200W

Phase after JWST Pupil   Intensity before NIRCam detector

Calculation with 20 wavelengths (1.76154 - 2.23846 um)
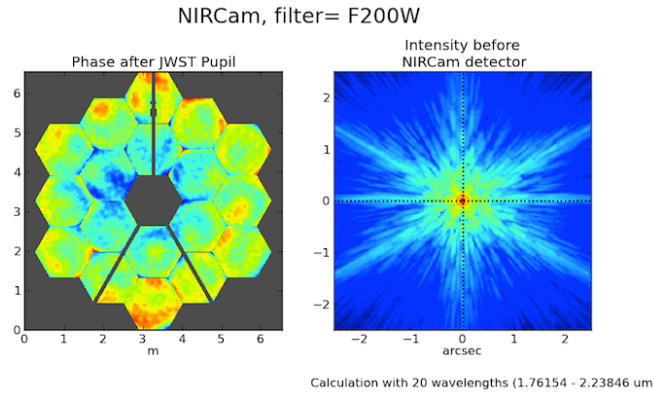
Figure 3: NIRCam F200W broadband PSF. The left panel shows the input phase on a linear scale, and the right panel shows the derived PSF on a log scale.

MIRI, filter= F1000W

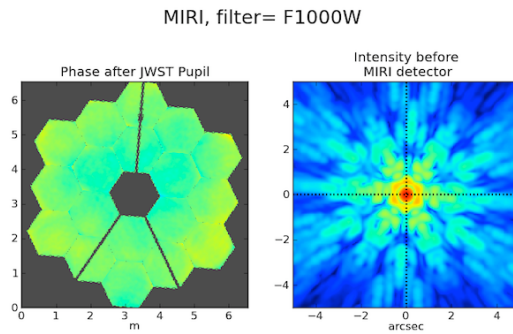Phase after JWST Pupil   Intensity before MIRI detector

Figure 4: Same as previous figure but for MIRI F1000W. Note that the input pupil is now rotated by ~ 4.5 degrees, matching the orientation of MIRI's field of view relative to JWST's pupil axes. The phase looks smoother, because at MIRI's longer wavelength a given absolute wavefront error corresponds to a smaller phase in waves. Likewise the PSF itself is also larger in angular scale due to the longer wavelength.

Check with the JWST SOCCER Database at: http://soccer.stsci.edu/DmsProdAgile/PLMServlet

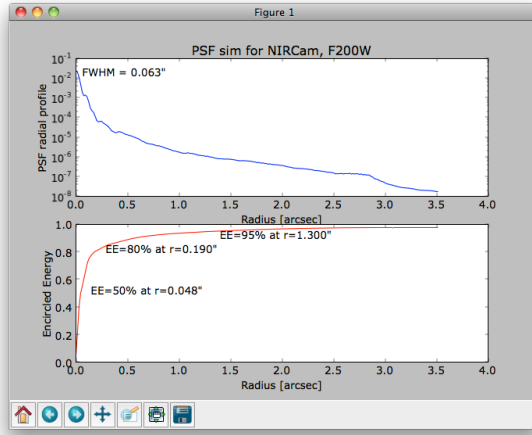To verify that this is the current version.

Figure 5: Derived radial profile and encircled energy for the NIRCam PSF shown in Figure 3.
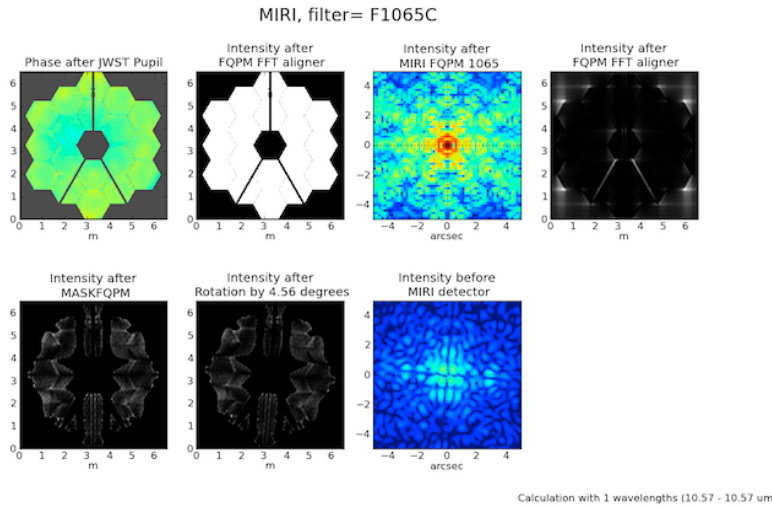

Figure 6: A more complicated calculation, in this case showing a MIRI coronagraphic PSF using the 10.65 μm quandrant phase mask. Each panel shows one step in the optical propagation through the system. The details of this calculation are discussed below in section 4.2.

4.0 Description of the Algorithms

The problem at hand is to transform supplied, precomputed OPDs (derived perhaps from a detailed optomechanical model of the telescope, or from Monte Carlo simulations consistent with the design requirements) into observed PSFs as seen with one or more of JWST's various detectors. This requires knowledge of the location and orientation of the detector planes, the properties of relevant optics such as bandpass filters and/or coronagraphic image and pupil plane masks, and a model of light propagation between them.

Check with the JWST SOCCER Database at: http://soccer.stsci.edu/DmsProdAgile/PLMServlet

To verify that this is the current version.

Instrumental properties are taken from project documentation and the published literature as appropriate; see the *References* appendix to the software manual for detailed provenance information. Optics may be described either numerically (for instance, a FITS file containing a mask image for a Lyot plane or a FITS bintable giving a spectral bandpass) or analytically (for instance, a coronagraph occulter described as a circle of a given radius or a band-limited mask function with given free parameters).

WebbPSF computes PSFs under the assumption that JWST's instruments are well described by Fraunhofer diffraction, as implemented using the usual Fourier relationship between optical pupil and image planes (e.g. Goodman et al. 1996).

4.1   Direct Imaging

Direct imaging calculations are fairly straightforward. Restating a fundamental result of Fourier optics: the complex amplitude of the electric field at the image plane, often termed the 'amplitude spread function', is given by the Fourier transform of the complex electric field at the input pupil. The point spread function for the intensity of electromagnetic radiation is given by the square of the amplitude spread function. Calculating such Fourier transforms is the heart of what WebbPSF does; it is simple conceptually, but there are a lot of subtle details (e.g. units, sampling, and normalizations) that must be handled correctly in a proper numerical implementation.

The familiar Fast Fourier Transform (FFT) algorithm often used for discrete Fourier Transforms imposes a specific fixed relationship between pixel sampling in the pupil and image planes:

$$\theta_{pixel} = \frac{\lambda}{N_{pixels\ in\ pupil\ array}} = \frac{\lambda}{D_{pupil} \times P}$$

where P is a padding factor for how large an array of zeros the actual pupil is embedded in. Obtaining finely sampled PSFs via an FFT thus requires transforming very large arrays consisting mostly of zero-padding, which is computationally inefficient in terms of both memory and processor cycles for cases where only a small region of the PSF is of interest. For instance to get pixels twice Nyquist sampled, size $\lambda/4D$, required P=4, so the pupil array is 15/16 just zeros. In cases where fine spatial structure in the pupil must be modeled, for instance JWST's segment gaps, this is a significant limitation. If we wish to place two pixels per ~7 mm segment gap, this requires ~2000 pixels across the JWST pupil, and thus ~256 MB per array for a twice Nyquist FFT. This is achievable on modern computers, but FFTing such an array is still quite slow.

A more computationally attractive method is to use a discrete matrix Fourier transform, which provides flexibility to compute PSFs on any desired output sampling without requiring any excess padding of the input arrays. While this algorithm's computational cost grows as *O(N^3)* versus *O(N log N)* for the FFT, we can generally get away with transforming much smaller arrays, in essence exchanging fast FTs of very large arrays for

moderate speed FTs of small ones. Furthermore, much of the FFT algorithm's apparent speed advantage is immediately lost due to the need to resample the output onto the real pixel grid, which is an *O(N^2)* operation.

We therefore implement a discrete matrix FT as the standard FT used for direct imaging calculation[1] in WebbPSF, following the specific matrix FT implementation outlined in Soummer et al. 2007. [2] The process of calculating a direct imaging PSF then becomes:

1. Determine the set of wavelengths and weights to compute, based on synthetic photometry for the selected input source and instrument filter transmission. This step uses the pysynphot synthetic photometry library, same as the HST and JWST ETCs.

2. Initialize an optical system model containing the desired OPD file and instrumental configuration such as detector pixel size.

3. Iterate through the set of wavelengths:

   a. Apply the OPD map to add wavefront error.

   b. Propagate to the detector pixel grid (optionally subsampled) using the matrix FT algorithm

   c. Sum results to an accumulator array.

4. If the user requested that both an oversampled image and a detector sampled image are produced, then rebin the oversampled array down to the detector resolution. Add this as a FITS image extension.

5. Save the output to disk as a FITS file.

4.2   Coronagraphy

Coronagraphic calculations are broadly similar to the direct imaging case, except propagation through multiple optical planes is required, typically input pupil, occulter plane, Lyot pupil, and detector. This is straightforward in principle, but often computationally demanding given the need for fine sampling in the image plane (e.g. to well represent the shapes of physically small occulters, which typically requires sampling much finer than the diffraction limited beam size). The method of calculation adopted varies depending on the type of coronagraph.

Lyot and Band-Limited Coronagraphs: Here a further optimization in calculation is possible using the semi-analytic coronagraphy algorithm of Soummer et al. 2007. This approach relies on Babinet's principle that the diffracted electric field amplitude resulting from light propagating past an opaque body (such as a coronagraph occulter) is identical

---

[1] Note that this also includes the case of non-redundant mask interferometry with TFI, which from a purely optical perspective is simply direct imaging with an unusual pupil geometry.

[2] Thanks to Anand Sivaramakrishnan for providing his original Python implementation of this algorithm, which we extended into a more flexible framework for use in the WebbPSF code.

except for sign from the diffraction pattern of a transparent hole of the same shape and size. Therefore instead of performing the full propagation of a beam past the occulter, we can instead propagate only the portion of the beam which blocks at the occulter, and then subtract it from the full wavefront at the Lyot plane. See Soummer et al. 2007 for algorithmic details. The semi-analytic algorithm is currently implemented for all TFI coronagraphs[3] and the NIRCam band-limited circular occulters (see section 4.4.1 for details). Test code verifies that the semi-analytic and classical methods yield identical results to within numerical precision.
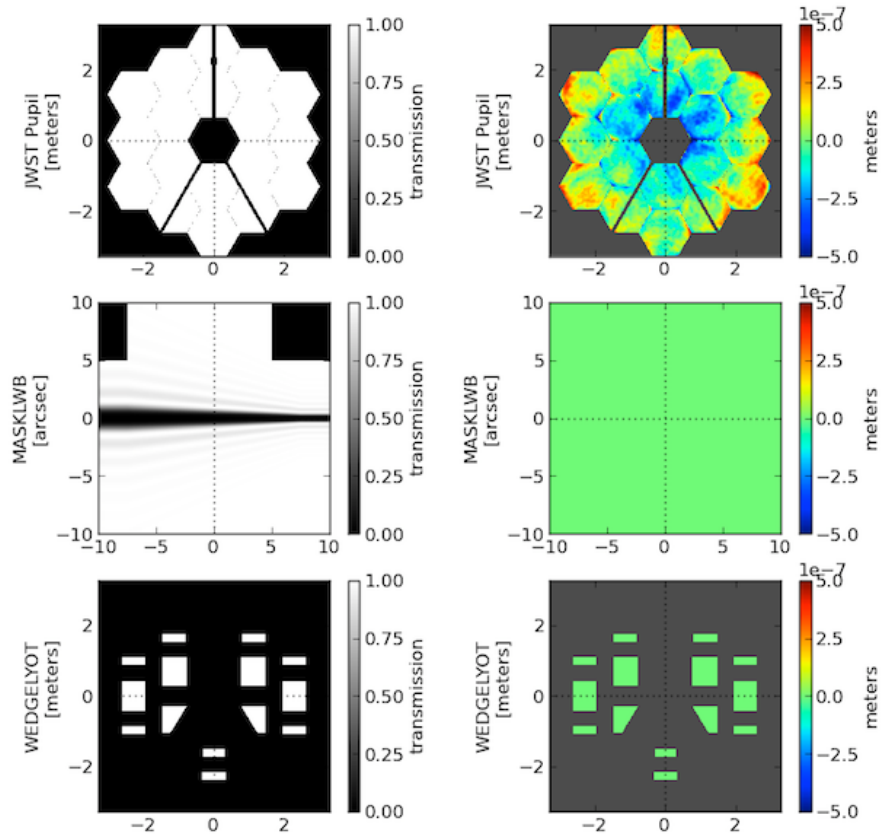

Figure 7: Coronagraphic optics models for NIRCam's long-wavelength bar occulter. From top to bottom the panels show the input OPDs, the image plane band-limited mask plus ND squares for acquisition, and the bar occulter Lyot mask.

---

[3] This technical report documents WebbPSF as developed for the original TFI design, prior to the etalon cancellation. A future update of this software will revise the TFI model in accordance with the nTFI design changes. The TFI/nTFI effort is discussed more below in section 4.4.4.

Four-Quadrant Phase Mask: The MIRI FQPMs are a different case. Because the image plane phase mask fills the entire field of view, it would be inappropriate to use the semi-analytic method. Instead, a classical FFT propagation is used, suitably zero-padded to achieve oversampling.

One complication is introduced here by the pixel alignment conventions adopted by the FFT algorithm. Typically, the FFT algorithm places the zero-order spatial frequency term in the (0,0) pixel – that is to say, a PSF calculated via an FFT will be centered on a pixel. However, for proper calculation of FQPM results, we need the PSF centered on the corner between four pixels, such that the central peak is equally and symmetrically spread between the four quadrants. To achieve this numerically using the FFT requires a wavelength-dependent tilt be added to the wavefront prior to the propagation to the image plane, then removed at the Lyot plane. The required tilt is

FFT_tilt = -1/2 * wavelength / (wavefront_diameter * oversample)

in both the X and Y directions. This is implemented using a virtual optic in the optical model called an 'FQPM FFT aligner'; this does not represent any physical object in the optical system, but in current versions of WebbPSF these optics will appear in onscreen displays (e.g. Figure 6 above).

4.3   Integral Field Spectroscopy

Integral field spectroscopy is not yet supported, but is planned for a future release. The expectation is that WebbPSF will produce an output datacube (x,y,wavelength) with a format similar to a single reduced IFS data frame, possibly at a reduced set of wavelengths. The details of this implementation remain to be finalized pending discussions with the NIRSpec and MIRI groups and the IFS Working Group at STScI.

4.4   Notes on Individual Instruments

4.4.1   NIRCam

The NIRCam model will automatically select the proper pixel scale for the SW or LW channel depending on the chosen filter. No differential WFE between the two channels is yet included, nor is there any difference between NIRCam A and B. (In fact, WebbPSF does not yet have any notion of there being two distinct NIRCam modules, a task left for a future version.)

NIRCam coronagraphic occulters and pupil masks were implemented following the descriptions given in Krist et al. 2008, 2010. Any details not clear from those papers were clarified via private communication with Krist.

Note that while the transmission profiles of band-limited occulters in theory extend infinitely from the origin, as fabricated in hardware for NIRCam the occulter profiles are truncated at the second transmission peak from the center (J. Krist, private

communication). This finite support allows the semi-analytic method to be applied usefully to their modeling, and this is currently implemented for the .

The NIRCam wedge occulters are currently implemented with classical propagation (using FFTs of zero-padded pupils to the full image plane array). They are in theory also capable of being calculated using the semi-analytic method, but doing so in a computationally efficient manner will require extending the matrix FT code to handle non-square arrays, which has not yet been completed. This is expected in a future release of WebbPSF.

4.4.2   NIRSpec

NIRSpec support is fairly rudimentary: just the two broadband target acquisition filters. These are called 'Broadband A' and 'Broadband B' in various NIRSpec documentation but I have opted to use the ST-style nomenclature 'F110W' and 'F140X'. There is no support for the optical effects of the MSA nor the IFS yet.

4.4.3   MIRI

MIRI coronagraphic optics were implemented based on their published specifications. Lyot mask designs and clarifications of details were provided by Anthony Bocaletti.

Impact of real vs. notional filter transmissions

For the initial software release of WebbPSF, the MIRI PIs requested that we not release the actual instrument throughput and filter transmission models but instead use simple square box transmission curves for each filter. To evaluate how much difference this makes to the results, I computed and compared PSFs using both the real filter curves (provided by pysynphot for the regular broadband filters, and provided by Christine Chen for the coronagraphic and ND filters) and notional top-hat function transmissions based on the nominal filter properties.

I find that the difference in PSF FWHM is generally less than 1.5%, and the difference in encircled energy at a radius of 1 arcsec is typically <1%, so the top-hat transmissions are acceptable for most modeling purposes today. The differences are most pronounced for the longer wavelength filters. In particular, the measured F1500W, F1800W, and F2100W transmissions are significantly wider than the nominal properties listed on the MIRI web site. For an assumed target with a Rayleigh-Jeans spectrum at these wavelengths, the increased throughput at shorter wavelengths causes the simulated PSFs using the measured curves to have narrower FWHM than the PSFs using the nominal properties. In the case of the F1800W filter, the measured curve yields FWHM=0.585" while the box profile filter yields FWHM=0.594", hence a 1.5% difference. The difference is mostly relocating light between the core and the Airy rings, but the overall encircled energy at an arbitrarily chosen radius of 1 arcsec doesn't change very much. See Figure 8. For the short wavelength or narrower coronagraphic filters there is little measurable difference (e.g. F1280W, real filter FWHM 0.417", box filter FWHM 0.415").
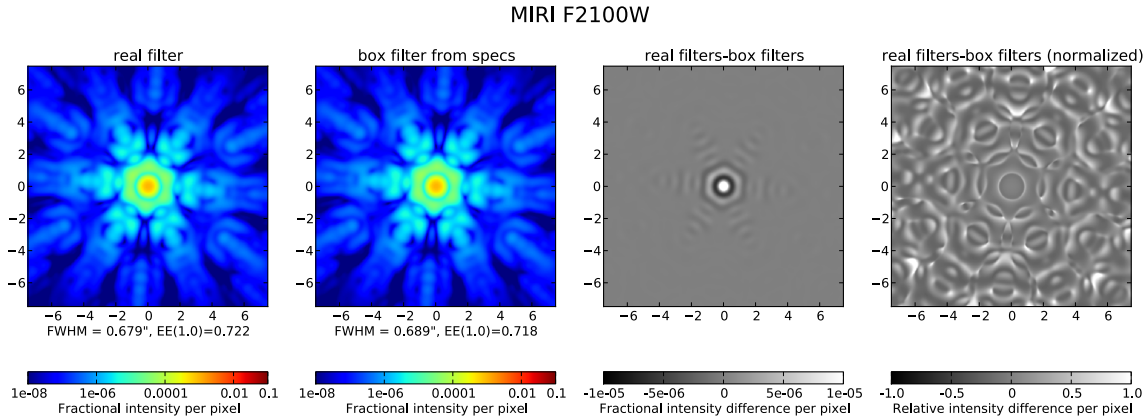
MIRI F2100W

Figure 8: Comparison of MIRI F2100W PSFs using measured and notional filter properties, for one of the cases with the largest differences.

4.4.4   TFI

WebbPSF was developed and initially released prior to the recent cancellation of the TFI etalon, and thus currently models the original design of TFI including the etalon. A future update to this software will reflect the revised "nTFI" optical design, hopefully including the grism modes.

While nTFI will retain the coronagraph occulting spots, because the Lyot stops are sacrificed to allow the insertion of the new grisms in the pupil wheel, coronagraphy with nTFI is not believed to be scientifically compelling and thus will not be developed. However, TFI coronagraphic simulations below in this document are retained for the historical record.

WebbPSF based its simulations of narrow-band imaging through the TFI etalon on a simulated Gaussian transmission profile with spectral resolution obtained from a lookup table of resolution versus wavelength provided by Alex Fullerton based on data from ComDev.

4.4.5   FGS

The FGS model is currently very rudimentary, just a top-hat filter transmission profile covering the full detector bandpass.

5.0 Steps Toward Improved Precision in PSF Simulations

5.1   Sampling Requirements for Numerical Accuracy

Obtaining high accuracy and precision in PSF calculations requires careful treatment of both the range of wavelengths included in the selected bandpass and also the subpixel sampling and integration onto the detector pixels. This section seeks to answer the

Check with the JWST SOCCER Database at: http://soccer.stsci.edu/DmsProdAgile/PLMServlet

To verify that this is the current version.

question "for a given desired degree of PSF accuracy, how finely must we sub-sample the wavelength range and pixel scale?" Because calculation time scales quadratically with pixel subsampling and linearly with wavelength sampling, it is desirable to use the minimum acceptable sampling that will yield the desired accuracy.

The wavelength-dependent change in position of any given PSF feature increases linearly with separation from the PSF center, and is proportional to the spectral bandpass. Thus the need for fine wavelength sampling should increase proportional to $\Delta\lambda \cdot r / (\lambda/D)$. In other words, *the larger a field of view one cares about or the broader a filter is used, the more finely the wavelength range must be sampled*.

On the other hand, pixel sampling matters most near the core of the PSF, where the flux is changing very rapidly on small spatial scales. Finer subpixel sampling also becomes increasingly important for shorter wavelengths which are not Nyquist sampled by a given detector. Thus, *the closer to the PSF core you care about fine structure or the shorter your central wavelength, the more finely sampled your PSF will need to be*. Because the NIRSpec, TFI, and FGS detectors sample the PSF relatively coarsely, they will require a higher degree of oversampling in simulations than NIRCam to reach a given SNR level. MIRI is fairly well-sampled.

> *Note:* WebbPSF makes no attempt to incorporate detector effects such as pixel MTF and interpixel capacitance that are independent of optical propagation effects. Simulations of such effects, if needed, should be added to WebbPSF outputs using dedicated detector simulation codes. Because WebbPSF allows arbitrarily fine sampling of its output images, this modular approach provides a straightforward path toward very precise modeling of detector effects such as intrapixel quantum efficiency variations.

Consider two types of measurement one might wish to make on the PSF:

- Measuring the encircled energy curve to a given precision
- Measuring individual pixel flux levels to a given precision in the PSF wings

The latter is a substantially more challenging measurement because it demands accuracy at a single pixel level rather than averaging across many pixels. Such a calculation might be motivated by, for instance, modeling coronagraphic PSF subtraction in which we seek to achieve 1-2 orders of magnitude reduction in the PSF wings. Accurately simulating that process demands a comparable level of fidelity in our PSF models. We thus evaluate below the number of {oversamplings, wavelengths} needed to achieve SNR=100 in a single pixel at a given radius (where SNR in this context is calculated as *(model-truth)/truth* on a per-detector-pixel basis). We also present tables giving the requirements for SNR=20 in a given pixel for less demanding modeling tasks.

To evaluate what levels of sampling are needed in practice, for each NIRCam and MIRI filter we first computed a very highly oversampled image (nlambda=200, oversampling=16; field of view 5 arcsec for NIRCam and 12 arcsec for MIRI), which we used as a "truth" image. (For practical purposes, we consider this level of sampling likely to be sufficiently fine that it can serve as a good stand-in for an infinitely sampled PSF, but this is an assumption we have not quantitatively validated. However, since there are >200 subsamples in both pixel and wavelength space and the maximum field positions considered are much less than 200 λ/D from the PSF center, the residuals ought to be of order <1/200 and thus these are sufficient for our purposes of testing SNR=100.)

We then computed a grid of simulated images for each filter using wavelength sampling ranging from 1 to 75 wavelengths per filter passband, and 1x, 2x, 4x, and 8x oversampling of pixel scale. (Note that "2x oversampling" means that a 2x2 grid of subpixels is computed per physical detector pixel, so the actual number of computed values scales as oversampling^2). For each image we then computed the difference image

$$Diff = \left| \frac{model - reference}{reference} \right|$$

and then evaluated the average absolute difference as a function of radius. For the <5 µm instruments we used test radii of 0.5, 1, 2, and 3", while for MIRI we used 1, 2, 3.5, and 5". Examples of these difference images are shown on the next two pages.

Tables on the subsequent pages list the minimum numbers of {oversampling, wavelengths} required to achieve differences less than 0.01 or 0.05 (SNRs of 100 or 20) in comparison with the very finely sampled reference images. In cases where none of the tested parameters were adequate (typically for near the core of undersampled wavelengths), the string "higher!" is printed. Users interested in SNR=100 simulations in such cases should investigate what oversampling >8x will meet their needs.

We adopted the default number of wavelengths for each filter based on the results of these calculations as follows, with defaults generally chosen to yield SNR=100 inside of 2" radius. These defaults are set in a `filters.txt` file in WebbPSF's data directory so users may easily change them if desired (and of course one may choose different settings for any given calculation). Default oversampling is set to 4 for all instruments.

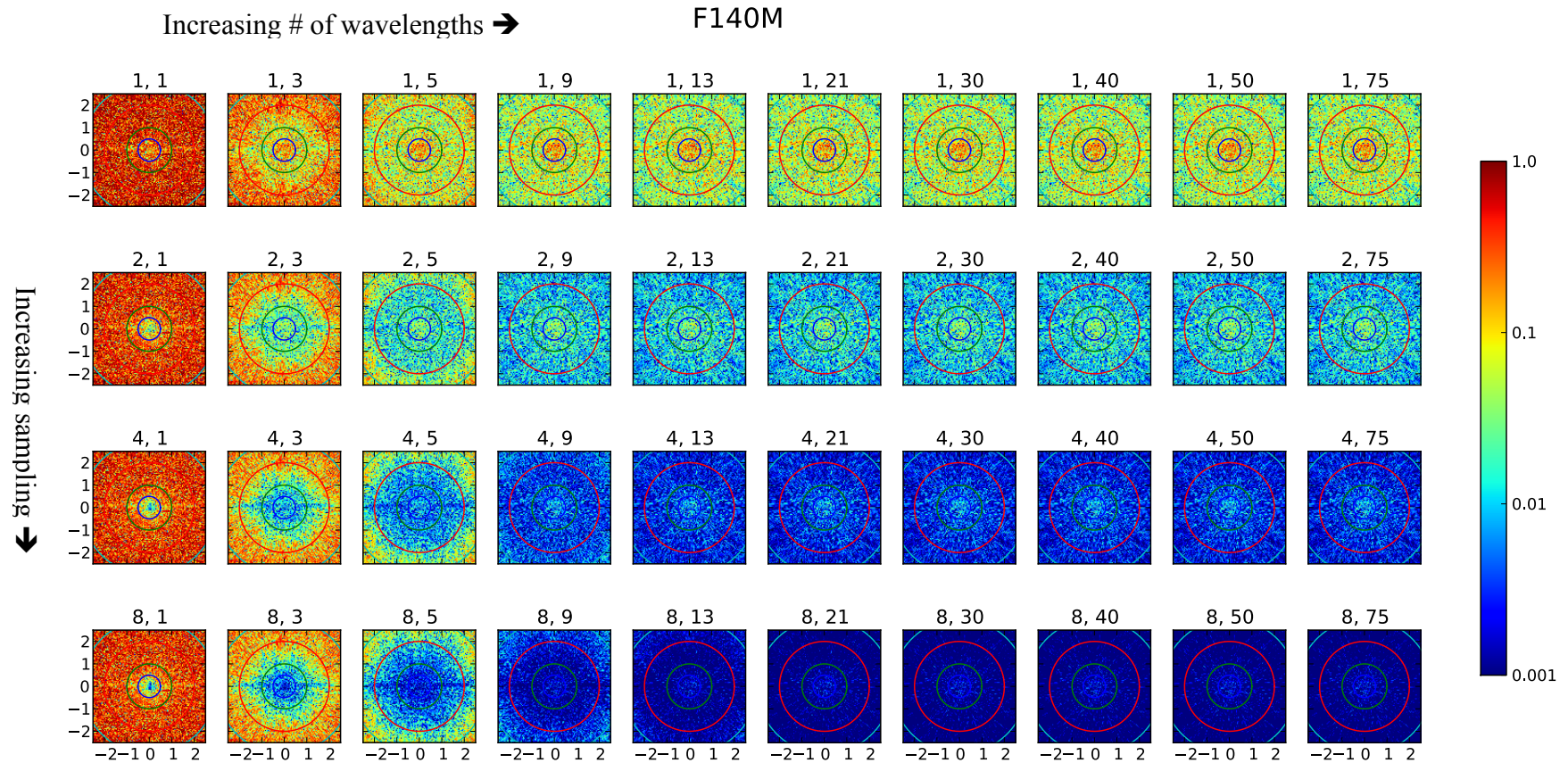| Instrument	Default number of wavelengths
NIRCam	Variable; typically 3 for narrow, 9 for medium, 20 for wide, 40 for double-wide.
NIRSpec	20 for F110W, 50 for F140X
TFI	3
FGS	20
MIRI	9 for all filters except 50 for the broad ND

Figure 9: Example of calculations to assess required sampling. Each panel shows the pixel-by-pixel difference from the reference PSF, labeled by (oversampling, # wavelengths) above each panel. Images are displayed on a logarithmic stretch from 1/1000 to 1 in relative error per pixel. The circles indicate radii of 0.5, 1, 2, and 3 arcseconds corresponding to the columns in the associated tables. This example for NIRCam's F140M filter shows that it requires 4x subsampling and 13 wavelengths in order to have the average relative error < 0.01 at a radius of 3". Thus a default sampling of 13 wavelengths was chosen for this filter.

Check with the JWST SOCCER Database at: http://soccer.stsci.edu/DmsProdAgile/PLMServlet
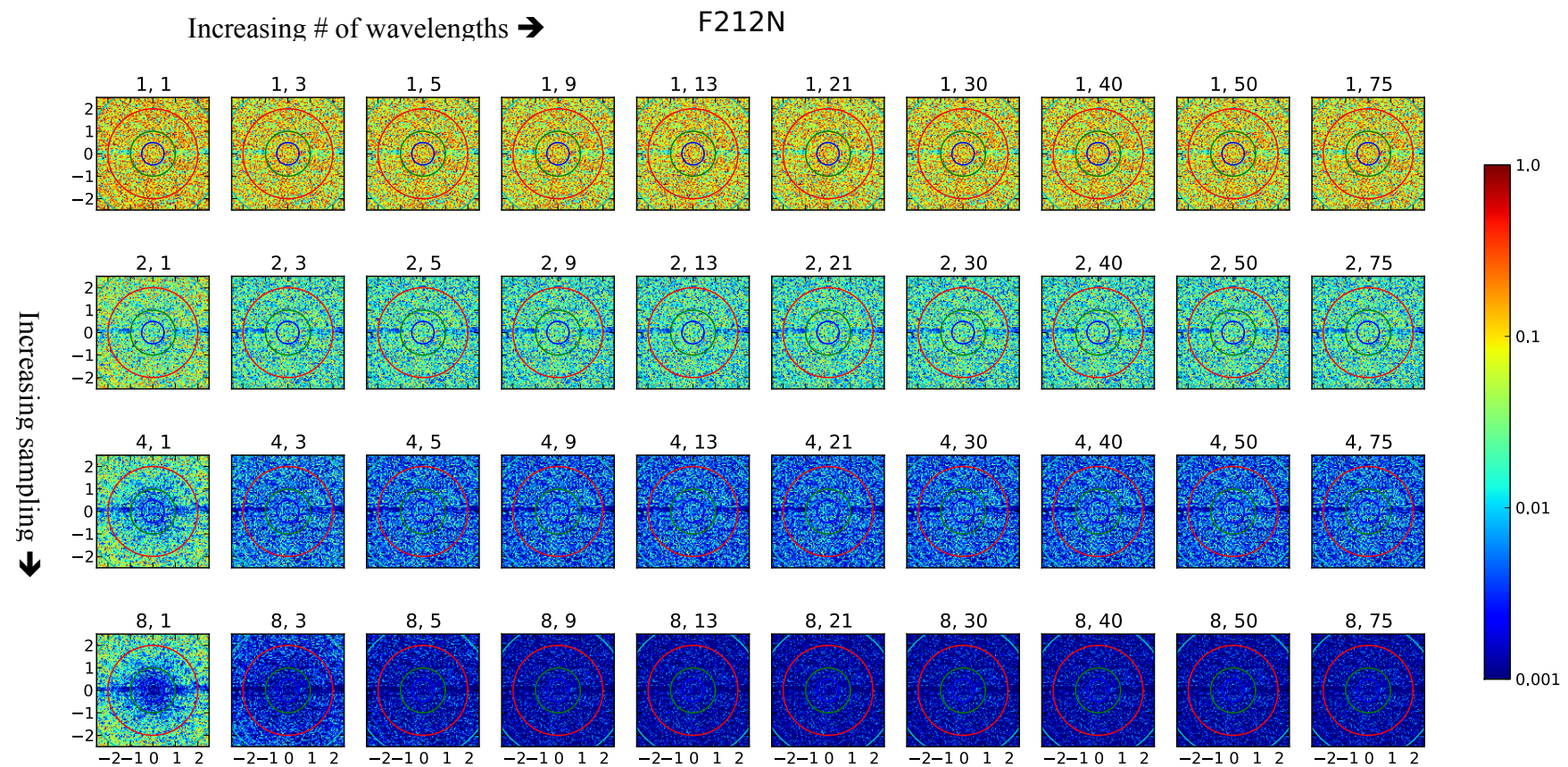
To verify that this is the current version.

Figure 10: Same as previous figure except for a narrow-band filter, F212N. In this case only 3 wavelengths are needed to achieve SNR>100.

NIRCam, SNR=100

Filter	r=0.5"	1.0"	2.0"	3.0"
F070W	higher!	(4, 13)	(4, 21)	(4, 30)
F090W	higher!	(4, 13)	(4, 21)	(4, 30)
F115W	higher!	(4, 9)	(4, 21)	(4, 30)
F140M	higher!	(4, 9)	(4, 9)	(4, 13)
F150W2	higher!	(4, 30)	(2, 75)	(2, 75)
F150W	higher!	(4, 9)	(4, 21)	(4, 21)
F162M	higher!	(4, 9)	(4, 9)	(4, 13)
F164N	higher!	(8, 3)	(8, 3)	(8, 3)
F182M	higher!	(4, 9)	(4, 9)	(4, 13)
F187N	higher!	(8, 1)	(4, 5)	(8, 3)
F200W	(8, 5)	(4, 9)	(2, 21)	(2, 30)
F210M	(8, 3)	(4, 5)	(4, 9)	(4, 9)
F212N	(8, 1)	(4, 3)	(4, 3)	(4, 3)
F225N	(8, 1)	(4, 3)	(4, 3)	(4, 5)
F250M	higher!	(8, 5)	(4, 13)	(4, 9)
F277W	(8, 5)	(4, 9)	(4, 13)	(4, 21)
F300M	(8, 3)	(8, 5)	(4, 9)	(4, 9)
F322W2	(8, 9)	(4, 21)	(4, 21)	(4, 30)
F323N	(8, 1)	(8, 1)	(8, 3)	(8, 3)
F335M	(8, 3)	(8, 5)	(4, 9)	(4, 9)
F356W	(8, 5)	(4, 9)	(4, 9)	(4, 13)
F360M	(8, 3)	(8, 5)	(4, 5)	(4, 9)
F405N	(8, 1)	(8, 1)	(4, 9)	(8, 3)
F410M	(8, 3)	(8, 5)	(4, 5)	(4, 9)
F418N	(8, 1)	(8, 1)	(4, 5)	(8, 3)
F430M	(8, 1)	(8, 3)	(4, 9)	(4, 9)
F444W	(8, 5)	(4, 9)	(4, 13)	(2, 21)
F460M	(8, 3)	(8, 5)	(4, 9)	(4, 9)
F466N	(8, 1)	(8, 1)	(4, 3)	(4, 9)
F470N	(8, 1)	(8, 1)	(4, 3)	(4, 3)
F480M	(8, 3)	(4, 21)	(4, 5)	(4, 9)

NIRCam, SNR=20

Filter	r=0.5"	1.0"	2.0"	3.0"
F070W	(8, 3)	(2, 9)	(2, 21)	(2, 21)
F090W	(8, 3)	(2, 9)	(2, 13)	(2, 21)
F115W	(8, 3)	(2, 9)	(2, 13)	(2, 21)
F140M	(8, 3)	(2, 5)	(2, 5)	(2, 9)
F150W2	(8, 9)	(2, 21)	(1, 50)	(1, 75)
F150W	(8, 3)	(2, 9)	(2, 13)	(2, 21)
F162M	(8, 3)	(2, 5)	(2, 5)	(2, 9)
F164N	(8, 1)	(4, 1)	(2, 3)	(4, 3)
F182M	(8, 3)	(2, 3)	(2, 5)	(2, 9)
F187N	(8, 1)	(4, 1)	(2, 3)	(2, 5)
F200W	(4, 3)	(2, 5)	(1, 13)	(1, 21)
F210M	(4, 3)	(2, 3)	(2, 5)	(2, 5)
F212N	(4, 1)	(2, 1)	(2, 3)	(2, 3)
F225N	(4, 1)	(2, 1)	(2, 3)	(2, 3)
F250M	(8, 1)	(4, 3)	(2, 5)	(2, 5)
F277W	(4, 3)	(2, 5)	(2, 9)	(2, 13)
F300M	(4, 3)	(4, 3)	(2, 5)	(2, 5)
F322W2	(4, 5)	(2, 9)	(2, 21)	(2, 21)
F323N	(4, 1)	(4, 1)	(4, 1)	(4, 1)
F335M	(4, 3)	(4, 3)	(2, 5)	(2, 5)
F356W	(4, 3)	(2, 5)	(2, 9)	(2, 9)
F360M	(4, 3)	(4, 3)	(2, 3)	(2, 5)
F405N	(4, 1)	(4, 1)	(2, 3)	(2, 3)
F410M	(4, 1)	(4, 3)	(2, 3)	(2, 5)
F418N	(4, 1)	(4, 1)	(2, 1)	(4, 1)
F430M	(4, 1)	(4, 3)	(2, 3)	(2, 5)
F444W	(4, 3)	(2, 5)	(1, 9)	(1, 13)
F460M	(4, 1)	(2, 5)	(2, 3)	(2, 5)
F466N	(4, 1)	(4, 1)	(2, 1)	(2, 3)
F470N	(4, 1)	(2, 3)	(2, 1)	(2, 1)
F480M	(4, 1)	(2, 5)	(2, 3)	(2, 3)

Check with the JWST SOCCER Database at: http://soccer.stsci.edu/DmsProdAgile/PLMServlet

To verify that this is the current version.

TFI, SNR=100

Filter	r=0.5"	1.0"	2.0"	3.0"
1.500um	higher!	(8, 3)	(8, 3)	(8, 3)
1.750um	(8, 3)	(8, 3)	(8, 3)	(8, 3)
2.000um	(8, 1)	(8, 3)	(8, 3)	(8, 3)
2.250um	(8, 3)	(8, 3)	(8, 3)	(8, 3)
2.500um	higher!	(8, 3)	(8, 3)	(4, 3)
3.000um	higher!	(8, 3)	(4, 5)	(4, 9)
3.250um	(8, 1)	(8, 3)	(4, 3)	(4, 3)
3.500um	(8, 1)	(8, 1)	(4, 3)	(4, 3)
3.750um	(8, 1)	(8, 3)	(4, 3)	(4, 3)
4.000um	(8, 1)	(8, 1)	(4, 3)	(4, 3)
4.250um	(8, 1)	(8, 1)	(4, 3)	(4, 3)
4.500um	(8, 1)	(8, 1)	(4, 3)	(4, 3)
4.750um	(8, 1)	(4, 3)	(4, 3)	(4, 3)
5.000um	(8, 3)	(8, 3)	(4, 5)	(4, 5)

TFI, SNR=20

Filter	r=0.5"	1.0"	2.0"	3.0"
1.500um	(8, 1)	(4, 1)	(4, 1)	(4, 3)
1.750um	(8, 1)	(4, 1)	(4, 1)	(4, 3)
2.000um	(4, 1)	(4, 1)	(4, 1)	(4, 3)
2.250um	(4, 1)	(4, 1)	(4, 1)	(4, 3)
2.500um	(8, 1)	(4, 1)	(4, 3)	(4, 3)
3.000um	(8, 1)	(4, 3)	(2, 3)	(2, 3)
3.250um	(4, 1)	(4, 1)	(2, 3)	(2, 3)
3.500um	(4, 1)	(4, 1)	(2, 3)	(2, 3)
3.750um	(4, 1)	(4, 1)	(2, 3)	(2, 3)
4.000um	(4, 1)	(4, 1)	(2, 3)	(2, 3)
4.250um	(4, 1)	(4, 1)	(2, 3)	(2, 3)
4.500um	(4, 1)	(4, 1)	(2, 3)	(2, 3)
4.750um	(4, 1)	(2, 3)	(2, 3)	(2, 3)
5.000um	(4, 1)	(2, 3)	(2, 3)	(2, 3)

MIRI, SNR=100

Filter	r=1.0"	2.0"	3.5"	5.0"
F560W	(4, 5)	(4, 9)	(4, 13)	(4, 13)
F770W	(4, 5)	(2, 9)	(2, 13)	(2, 21)
F1000W	(4, 3)	(4, 5)	(2, 9)	(2, 9)
F1065C	(4, 3)	(4, 5)	(4, 5)	(2, 5)
F1130W	(4, 3)	(4, 5)	(2, 5)	(2, 5)
F1140C	(4, 3)	(4, 3)	(4, 5)	(2, 5)
F1280W	(4, 3)	(2, 5)	(2, 9)	(2, 9)
F1500W	(4, 3)	(2, 5)	(2, 9)	(2, 9)
F1550C	(4, 3)	(2, 3)	(2, 3)	(2, 5)
F1800W	(2, 3)	(2, 3)	(2, 9)	(2, 9)
F2100W	(2, 3)	(2, 5)	(2, 9)	(1, 9)
F2300C	(2, 3)	(2, 5)	(1, 9)	(1, 9)
F2550W	(2, 3)	(1, 5)	(1, 9)	(1, 9)
FND	(2, 30)	(2, 40)	(2, 50)	(2, 75)

MIRI, SNR=20

Filter	r=1.0"	2.0"	3.5"	5.0"
F560W	(2, 3)	(2, 5)	(2, 9)	(2, 9)
F770W	(2, 3)	(1, 9)	(1, 9)	(1, 9)
F1000W	(2, 3)	(1, 5)	(1, 5)	(1, 5)
F1065C	(2, 1)	(2, 3)	(2, 3)	(1, 3)
F1130W	(2, 1)	(2, 3)	(1, 3)	(1, 3)
F1140C	(2, 1)	(2, 3)	(1, 3)	(1, 3)
F1280W	(2, 3)	(1, 3)	(1, 5)	(1, 5)
F1500W	(2, 3)	(1, 3)	(1, 5)	(1, 5)
F1550C	(2, 1)	(1, 3)	(1, 3)	(1, 3)
F1800W	(1, 3)	(1, 3)	(1, 5)	(1, 5)
F2100W	(1, 3)	(1, 3)	(1, 5)	(1, 5)
F2300C	(1, 3)	(1, 3)	(1, 5)	(1, 5)
F2550W	(1, 3)	(1, 3)	(1, 3)	(1, 5)
FND	(1, 13)	(1, 21)	(1, 40)	(1, 50)

Check with the JWST SOCCER Database at: http://soccer.stsci.edu/DmsProdAgile/PLMServlet

To verify that this is the current version.

5.2   JWST Pupil shape

The JWST pupil shape changed between OTE error budget Revision T and Revision V. The principle changes are a decrease in the inter-segment gap size and the addition of the secondary tower deployment hinge, which causes a slight bulge halfway down the +V2 secondary support.

Because the pupil gaps are small compared to the pixel scale in the 1024x1024 OPDs currently available, they are hard to represent well digitally. The segment gaps in the Revision T pupil are about 3 pixels across (~2 cm) while the Rev V design shrinks the gaps to 1 pixel (~7 mm), which more accurately reflects the planned inter-segment gap based on the OTE specification. The larger gaps in the earlier model were probably an attempt to capture the 'turned-down edges' around each PMSA but those are better represented as phase artifacts in the OPDs since they will in fact be gold coated and reflective. As the below figures show, the difference between the Rev T and V pupils causes noticeable changes in the amount of power in the PSF wings at large separations. This is as expected; recall that high spatial frequency (fine scale) pupil structure corresponds to large angular separations in the image plane.

There are two straightforward paths available to representing the pupil with higher fidelity. One approach would be to use a greyscale rather than binary pupil mask, using values between 0 and 1 to represent pixels which are only partially within the pupil aperture. Alternatively, a larger scale pupil file would allow better representation of fine structure. Use of both methods together can provide the highest fidelity. The non-FFT discrete Fourier transform algorithms implemented in WebbPSF will allow the use of larger arrays to remain computationally tractable.
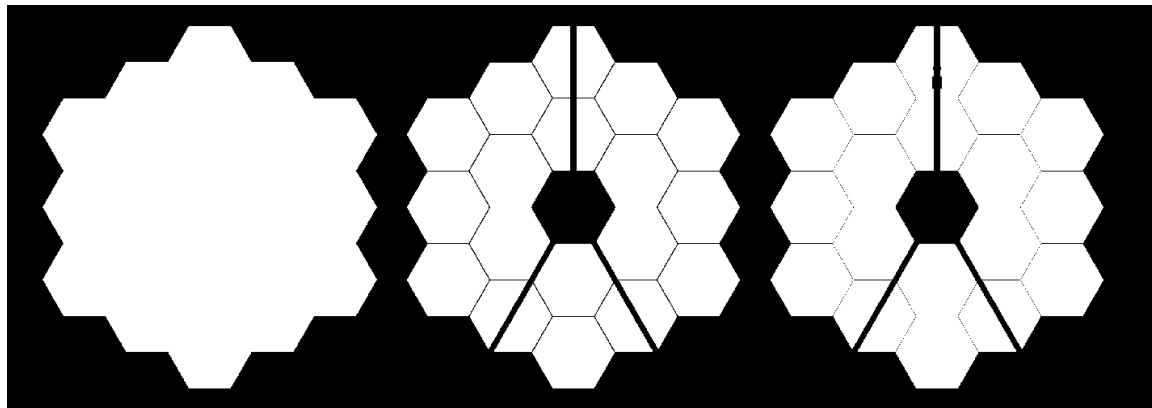
Figure 11: Pupil shapes for JWST. From left to right the exterior "tricontagon" outline of the pupil , and the Rev T and Rev V pupils.
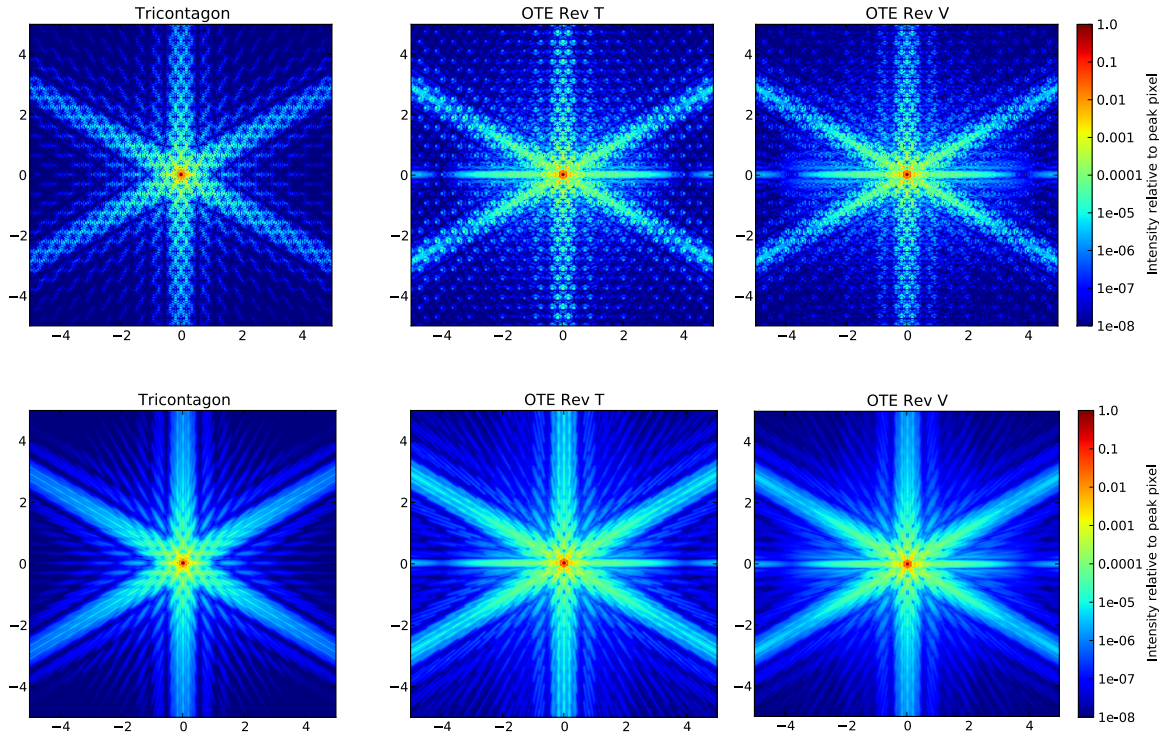
Figure 12: ... lti... g from different ... o ght the tricontag... an... V pupils. Top-r... u... bottom row is F20... cr... ate a strong hor... a...l power into the ±3... l c... secondary PSE... p... Re... V pupil compared t... re... uced gap width b... g...
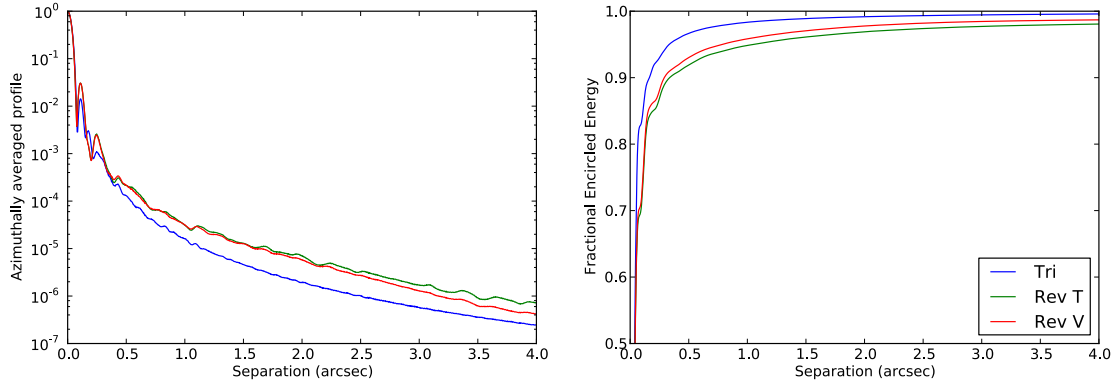

Figure 13: Radial profile and encircled energy for different pupil shapes. These profiles correspond to the broadband F200W datasets from the previous figure. The Revision V pupil's PSF has less intensity in its wings compared to Revision T.

6.0 Validation Tests

We now describe testing to verify WebbPSF's performance, both on its own and in comparison with other simulation codes.

6.1   Automated Software Validation via Unit Testing

WebbPSF includes an automated test suite built using the Python standard library's `unittest` module, which runs test code and checks the output against predefined success conditions. By having a large test suite we enable regression testing of any code changes made to WebbPSF: any edits that accidentally introduce subtle bugs which might slip by a human tester will hopefully be caught via one of the automated tests, and can then be fixed. See http://software-carpentry.org/4_0/test/ for more details on software testing philosophy and practices.

The following test suite exercises most functionality of WebbPSF and the underlying POPPY optical propagation library, with the exception of the GUI. `Test_poppy.py` validates the basic wavefront propagation code behaves properly, as follows. Most of these test cases are iterated at multiple wavelengths.

1. Check output file field of view matches requested field of view.
2. Verify basic functionality of AnalyticOpticalElement classes for e.g. circular aperture, scalar transmission, thin lens, etc.
3. Compute PSFs for circular, square, and hexagonal apertures. Verify the circular aperture PSF matches the analytic Airy function.
4. Verify PSF normalization works properly and conserves flux for FFT, MFT, and inverse MFT propagation methods.
5. Basic coronagraphy test: For zero input WFE, verify the wavefront at the Lyot plane is essentially all real (has a negligible imaginary part)
6. Test 'FQPM FFT Aligner' code for half-pixel alignment.
7. Test ideal FQPM; verify final image plane flux is suitably low on-axis while far off-axis sources are unaffected.
8. Test shifting point sources by tilting the incoming wavefront; point source should move to the requested location. Test iterates to check multiple position angles and offsets. Also validates that varying the amount of array zero-padding for oversampled FFTs does not affect source location.
9. Test NIRCam band-limited coronagraph occulters; verify occulted source flux is suitably low.
10. Validate semianalytic coronagraph code versus classical FFT propagation; ensure the outputs are identical to within machine precision (<1e-8).

`Test_webbpsf.py` repeats a similar set of tests, applied at a higher level via the webbpsf interface.

1. Verify output field of view is as requested, including specification via arcsec or npixels. Also check the even/odd parity option works properly with pixel oversampling. Repeat these checks for all instruments.
2. Verify offset sources appear in the correct position in the image plane. Repeat for NIRCam and MIRI at multiple position angles and separations.
3. Test coronagraphic propagation for MIRI and NIRCam

6.2 Comparison with JWPSF

The following tests demonstrate that WebbPSF produces PSFs that are consistent with those produced by JWPSF (Cox & Hodge, 2006). The PSFs are not *identical*, but the differences observed are all understood and directly due to the known ways in which WebbPSF improves on JWPSF. In particular:

- JWPSF assumes an NIRCam pixel scale of 0.034 arcsec/pix; WebbPSF by default uses an updated 0.0317 arcsec/pix value. For the purpose of these direct comparisons, we configured WebbPSF to use the same pixel scale as JWPSF.

- JWPSF uses the older Revision T OPDs, while WebbPSF uses Revision V by default. Likewise for these comparisons we configured WebbPSF to use the same Revision T OPDs as JWPSF.

- JWPSF uses much coarser wavelength sampling than WebbPSF by default.

We computed PSFs using both packages for NIRCam F200W and MIRI F1000W using the first available Revision T OPD for each included with JWPSF. We also computed perfect NIRCam F200W images using zero OPD.
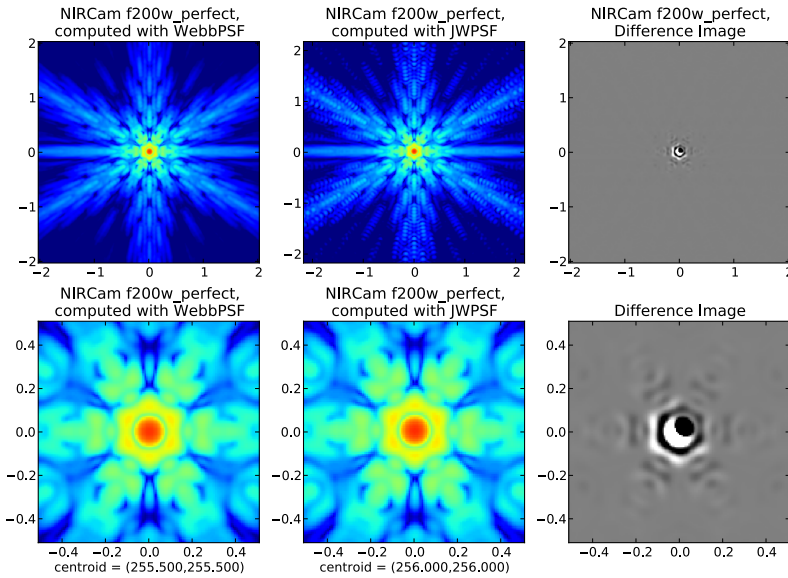
Figure 14: NIRCam F200W perfect PSF comparison with JWPSF. The color plots are shown on the standard log scale. The lower row shows a zoomed in region at the center of the PSFs shown in the top row. The right-hand column shows the difference of the PSFs scaled linearly from -1e-4 to 1e-4.

Figure 14 shows the simulated PSFs in the zero OPD case. The PSF structure is visually indistinguishable between the two codes near the PSF centers, but beyond several arcseconds the inadequate default wavelength sampling in JWPSF is obvious.

The difference image however reveals a systematic offset between the two near the PSF centers, akin to a difference in PSF centering. This is understood as a result of the way the two codes perform Fourier propagation. Both simulations were done to produce 512x512 pixel output images. The FFT propagation used in JWPSF places the zero-order Fourier component, and thus the PSF center, on a specific pixel (256,256). In contrast, the more flexible matrix FT in WebbPSF allows the PSF to be precisely centered around the middle of the array, split equally between the four central pixels at the true center of a 512x512 array. Thus it has centroid (255.5, 255.5).

To verify this, a half-pixel offset in both X and Y was applied to the WebbPSF model options. The resulting images in Figure 15 show that the simulated PSFs are then coaligned. There are still some remaining differences, visible as an Airy-ring like pattern. These are probably due to differences in wavelength sampling and weighting between the two (JWPSF using top-hat filter profiles while WebbPSF uses measured filter transmission curves).
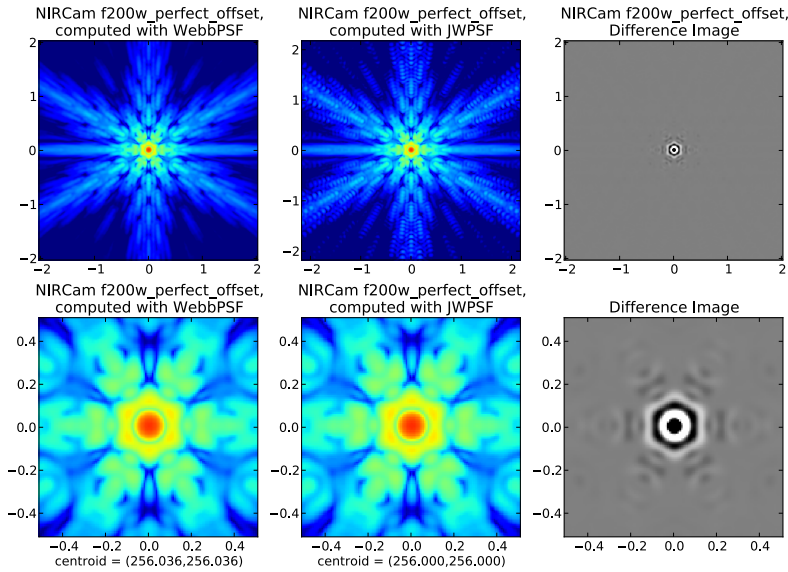
Check with the JWST SOCCER Database at: http://soccer.stsci.edu/DmsProdAgile/PLMServlet

To verify that this is the current version.

Figure 15: Same as previous figure, except a half-pixel offset has been applied in the WebbPSF model to align it with the JWPSF one.
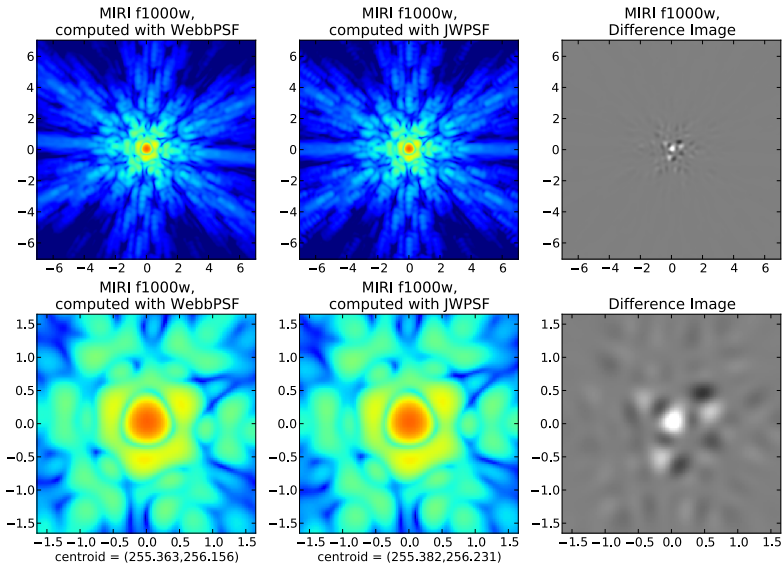

Figure 16 shows simulated MIRI F1000W PSFs using the Revision T OPDs, with the same half-pixel offsets applied to force alignment. The apparent PSF structures are very similar, indeed visually identical, but again there are minor differences typically <1e-4 of the total PSF intensity. These are likely due to a combination of

1) Different wavelength weightings based on top-hat (JWPSF) vs measured (WebbPSF) filter transmission functions.

2) Sampling and interpolation artifacts arising from slight differences in precisely where the programs sample the PSFs. Note that JWPSF calculates PSFs on a pixel scale that is fixed in lambda/D units, thus varies with wavelength, and then uses spline interpolation to resample these results onto the detector pixel grid. In contrast WebbPSF computes PSFs directly on the detector pixel scale or a subsampled version thereof.
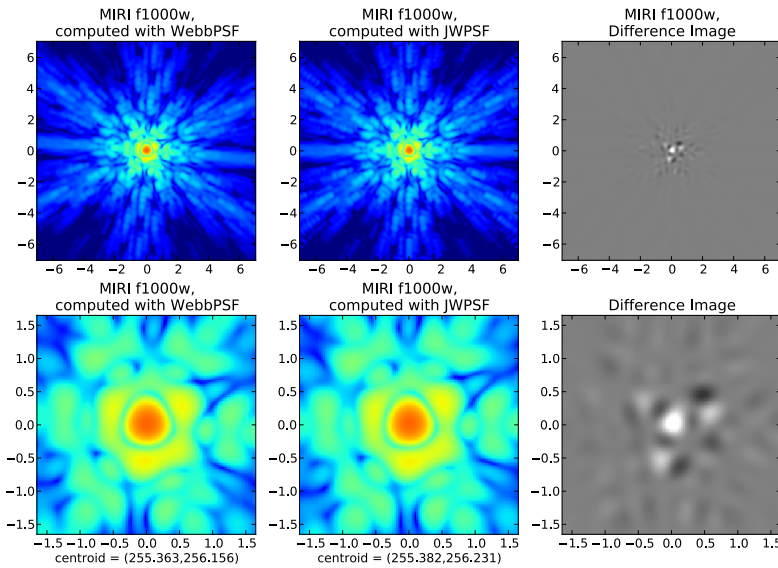
Figure 16: MIRI F1000W PSFs from a Revision T OPD. These show only small residuals.

6.3   Comparison with models in Makidon et al. 2007

In their discussion of JWST PSFs, Makidon et al. present plots of PSF FWHM and encircled energy derived from JWPSF simulations of NIRCam (Figures 6 and 7, Makidon et al. 2007). We reproduce this calculation and compare to their results here.
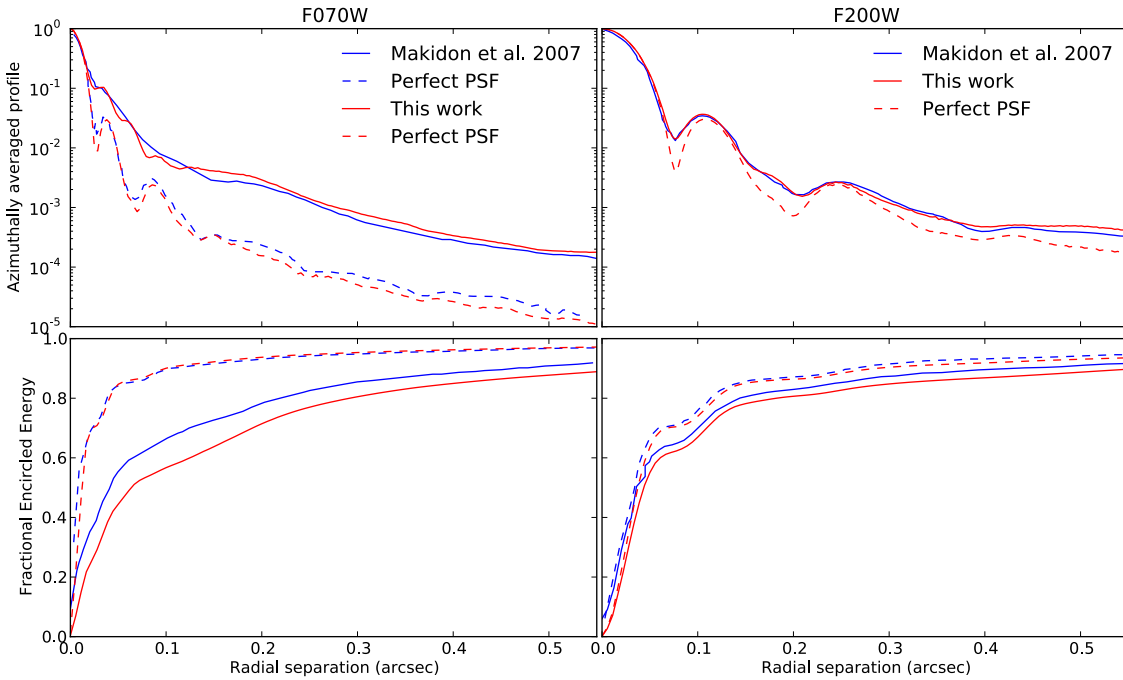
Figure 17: Comparison with PSF properties from Makidon et al. 2007 Figure 6. Azimuthally averaged profiles (top) and encircled energy (bottom) for representative NIRCam filters. The dashed lines show the PSFs with no wavefront error, the solid curves show RevT/RevV OPDs for Makidon et al. and this work respectively.

We begin with a comparison of F070W and F200W PSFs to the profiles shown in Figure 6 of that work. The PSF radial profiles are very similar overall, though there are small differences which are plausibly due to the differences in assumed OPDs and filter + instrument transmission profiles. The encircled energy curves are very similar for both filters in the case of the perfect PSFs. However, the profiles for the cases with nonzero WFE do not agree as well, differing by what appears to be a constant offset at large separations. This is again likely due to the different OPDs used. However, we note that, surprisingly, the encircled energy curves from Makidon et al. do not reach zero at the origin, at least not at the resolution it was possible to trace from their bitmap figure, so it is possible that some systematic differences were introduced by the limited resolution.

In any case, these PSFs are sufficiently similar to be within the expected uncertainties.
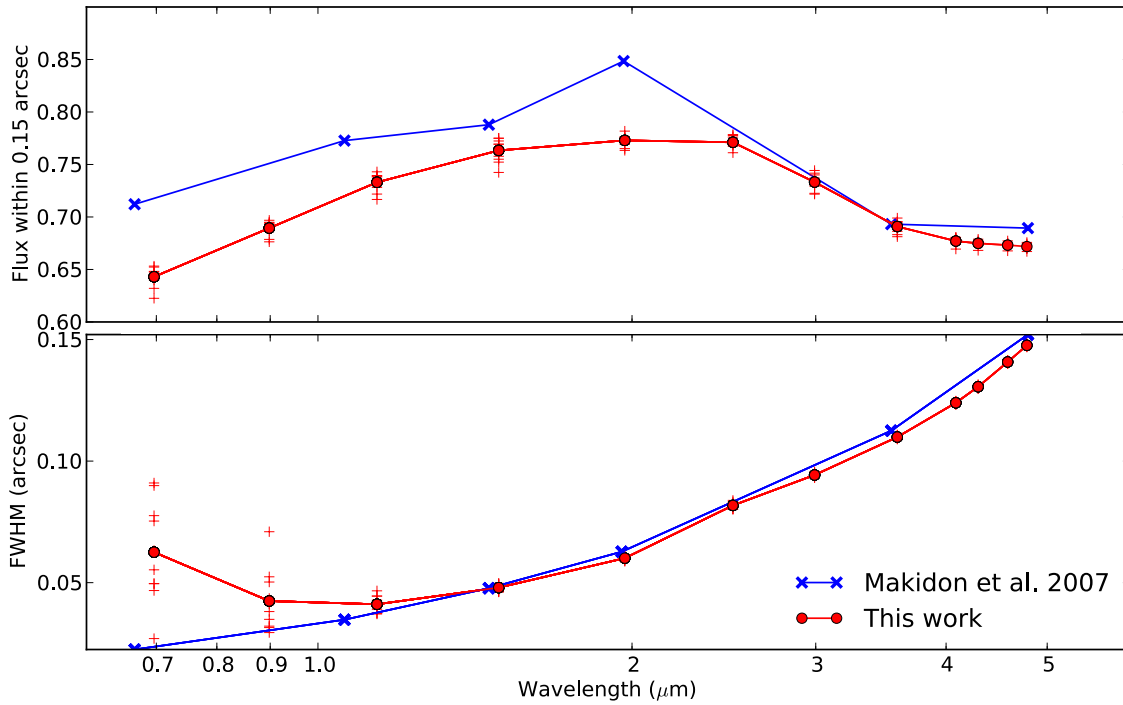
Figure 18: Comparison with PSF properties from Makidon et al. 2007 Figure 7. (Top) Encircled energy (as a fraction of the total flux) within a 0.15" radius. (Bottom) FWHM of the PSF. The red crosses show the individual measurements made using 10 simulated PSFs using 10 distinct Rev. V OPDs, and the red circles and solid line show the mean of these measurements. Differences between the OPDs are most significant at short wavelengths, as expected.

Their Figure 7 plots derived PSF properties versus wavelength, and again the results are similar but not identical. The fraction of total flux within a 0.15" radius (hereafter "EE(0.15)") is systematically lower for the current models with WebbPSF, although the values are very close for wavelengths > 2.5μm. The reason for the systematic difference in EE(0.15) at shorter wavelengths is not immediately apparent but may relate to the difference between the Revision T and V OPDs. The above calculation uses Revision V OPDs including the expected WFE from the OTE+ISIM, NIRCam's internal WFE, and a defocus term modeling jitter, yielding 155 nm RMS. No information is provided about which specific terms were included in the PSFs used by Makidon et al. I repeated the above calculation using the best available OPDs (OTE+ISIM only, no jitter and no NIRCam internal, yielding 123 nm RMS), but this increases EE(0.15) by only 1-2%, not enough to remove the discrepancy.

The agreement for the FWHMs is very good. At short wavelengths, the current WebbPSF average FWHMs bend sharply upwards as PSFs depart from diffraction limited below 1μm. However, the best-case FWHMs (lowest red crosses) are in excellent agreement

Check with the JWST SOCCER Database at: http://soccer.stsci.edu/DmsProdAgile/PLMServlet

To verify that this is the current version.

with the Makidon et al. results, suggesting they were indeed using an OPD that is at the optimistic end of the range included in the Rev V sims. Beyond ~1.5 μm, the WebbPSF FWHMs are systematically lower than the Makidon et al. values by 5-10 mas. This is very likely to be due to the use of real filter transmission profiles here versus box filters in JWPSF; see Section 4.4.3 which shows differences of this magnitude in MIRI PSFs using measured versus nominal filter properties.

6.4   Comparison with NIRCam Science Team Published Results

John Krist of the NIRCam science team provided two simulations of coronagraphic imaging performance with NIRCam in the ideal, zero-WFE case. These simulations include the occulted on-axis and the off-axis PSFs for both the 430R large circular occulter and the LWB long-wavelength bar occulter.

An initial comparison of Krist's simulations with WebbPSF models for the same case identified some small but significant differences, which were tracked down to

1) small differences in the width parameter describing the occulter shape, due to limited number of significant figures in the published description of the occulters. This was fixed by adjusting the BLC widths by about 1% to bring them into agreement.
2) An bug in WebbPSF's initial band-limited coronagraph model in which the transmission function for wavefront intensity was applied to wavefront amplitude, which has since been fixed. Note that the occulter profiles as specified in the NIRCam coronagraph papers by Krist et al. are stated in terms of intensity, so the square root must be taken before applying to the field amplitude.

With these fixes in place, excellent agreement was obtained between the WebbPSF and Krist simulations of NIRCam coronagraphy. See Figures 19 and 20. The results are essentially identical except for very small differences (<1e-7 of the flux) near the PSF core which are likely due to slightly different PSF sampling and interpolation choices.
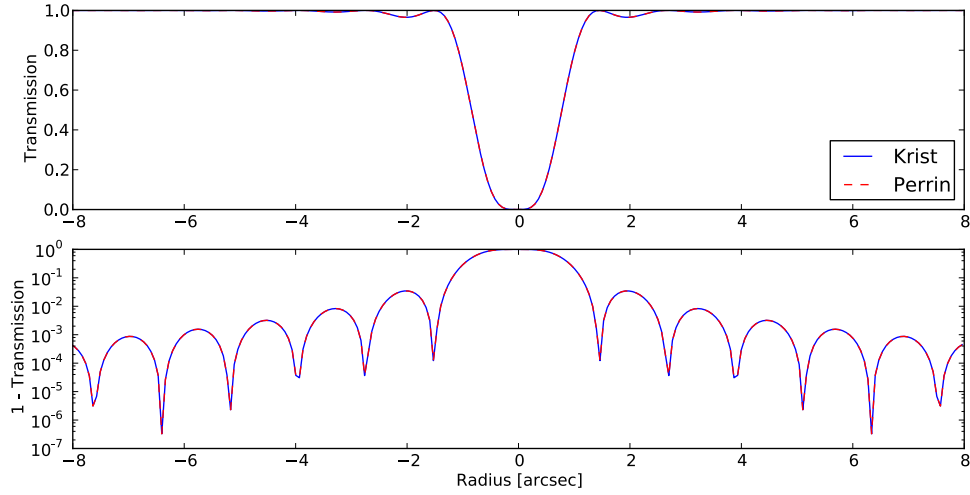
Figure 19: Comparison of transmission profiles for the MASK430R 4.3 μm circular occulter. The profiles are identical to within numerical precision (10e-10) .
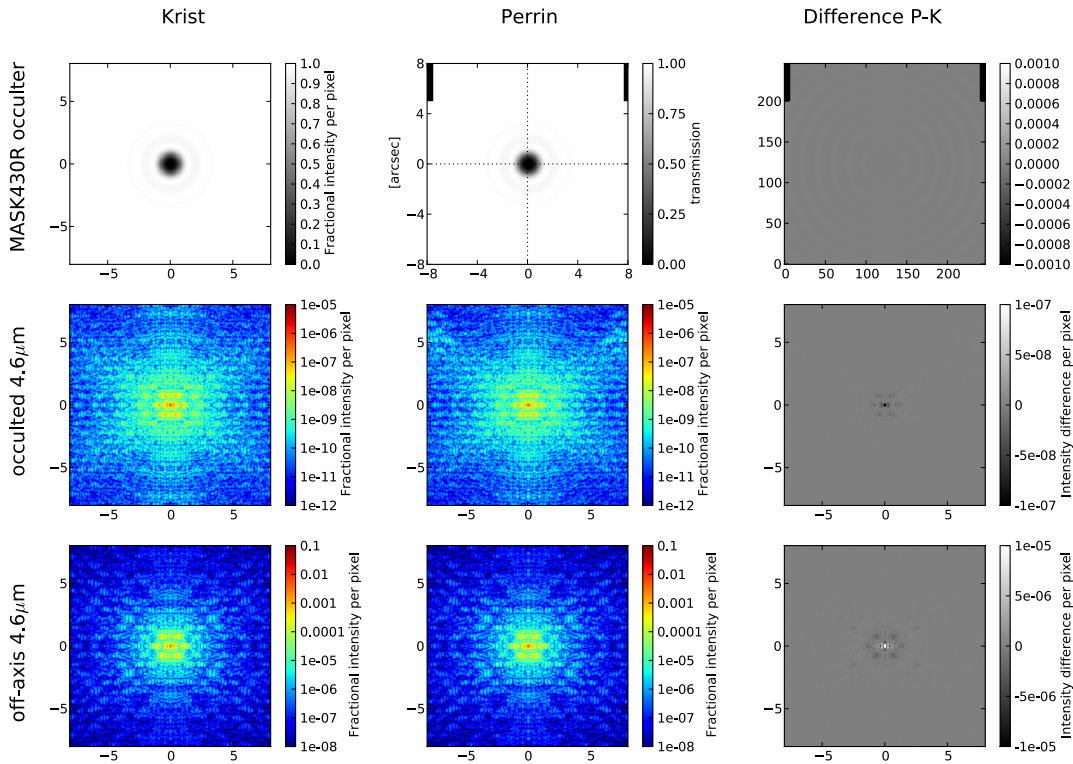

Figure 20: Comparison of coronagraphic simulations for the zero-WFE case, for the 430R occulter.

Check with the JWST SOCCER Database at: http://soccer.stsci.edu/DmsProdAgile/PLMServlet

To verify that this is the current version.

6.5 Comparison with MIRI Coronagraphic Target Acq Simulations by Remi Soummer

One of the primary applications of WebbPSF in the near future is expected to be simulations of coronagraphic target acquisition as part of studies done by the Coronagraphs Working Group. The most challenging case is likely to be the MIRI FQPM. We therefore demonstrate here that WebbPSF yields results consistent with those of a Mathematica-based MIRI coronagraphic simulation package developed by Remi Soummer.

The issue at hand is to understand how centroids become biased for targets close to the coronagraph occulter. To evaluate this, a series of MIRI coronagraphic simulations was created using the neutral density acquisition filter (FND) with the 10.6 µm FQPM, with the target star placed at a series of positions ranging from 0.005 to 2 arcseconds from the FQPM center at a position angle of 45º. The apparent centroid of the PSF can then be measured using the floating box centroid algorithm adopted for use on acquisition imagery by the JWST flight software (See Valenti 2007, JWST-STScI-001057).

Such calculations were first performed by R. Soummer and presented to the Coronagraphs Working Group, and are available in a draft document posted to the Coronagraph Working Group team web site. The relevant figures are reproduced below in Figure 22. These calculations were made using two independent codes, JWcorPSF and a Mathematica coronagraph model developed by Soummer, both of which used the Rev T OPDs.

WebbPSF was used to reproduce this calculation, with results as shown in Figure 21. Again the data are in very good agreement: Both models show consistently that discrepancies between the measured and correct PSF centroids arise due to the FQPM. The centroid discrepancies are largest between 0.2-0.3 arcsec from the FQPM center, reaching a maximum value of ~70 milliarcsec. The differences between the Soummer results and WebbPSF results is within the uncertainty arising from the different OPDs used. We conclude that the WebbPSF simulations have provided an independent verification of the results of Soummer, and support the conclusions reached about the MIRI target acquisition process as discussed in his draft technical report.

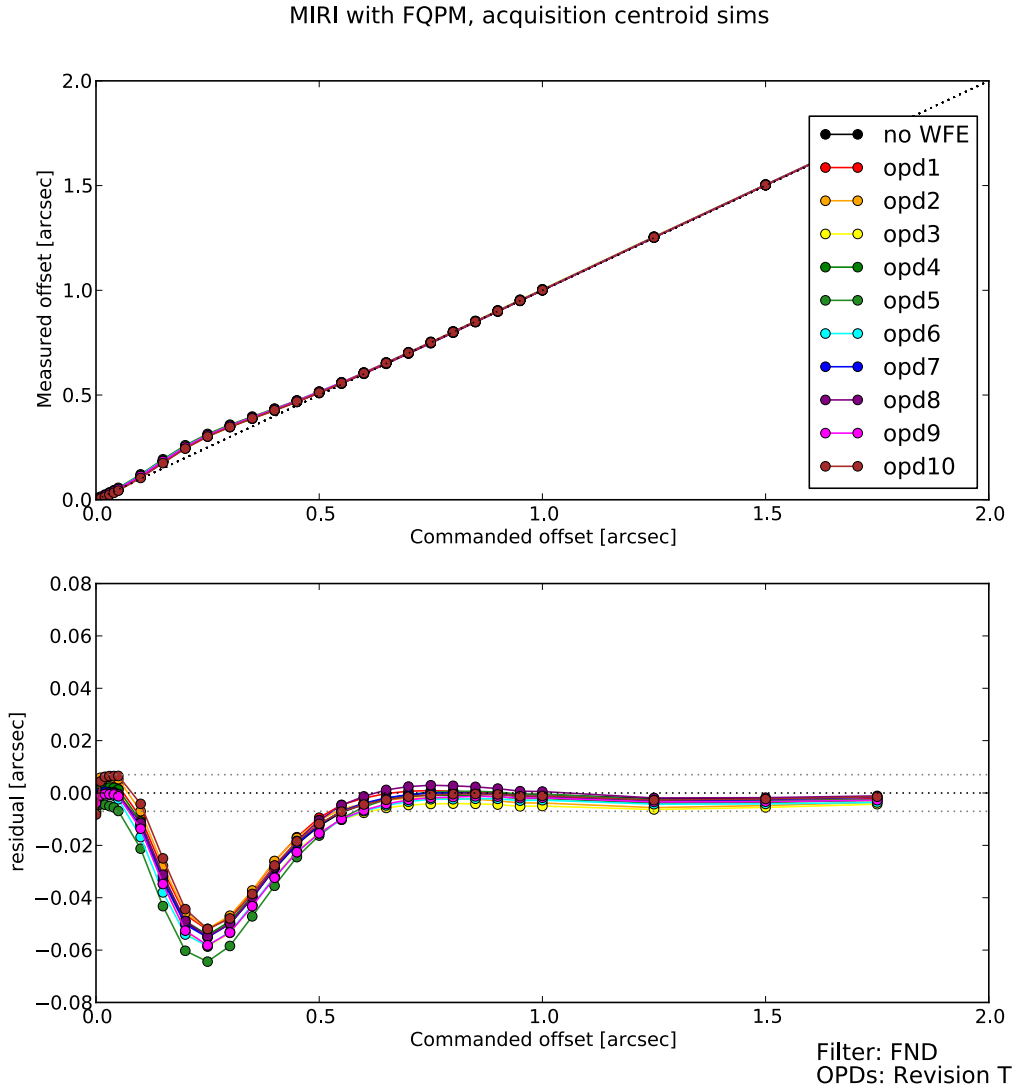MIRI with FQPM, acquisition centroid sims

Figure 21: MIRI coronagraphic acquisition simulations, for comparison with Figure 22. Top panel: Measured centroids using the floating-box centroid algorithm versus the true position of the star relative to the center of the FQPM. The dotted line corresponds to a perfectly accurate centroid measurement, and the colored lines show the 10 available Rev V OPDs. Bottom panel: Difference between true position and the measured position, for the same simulations. To avoid erroneous centroid measurements, the separation must be at least 0.6-0.7" and preferably more than 1 arcsecond. The horizontal dotted lines indicate the ±7 mas tolerance desired.
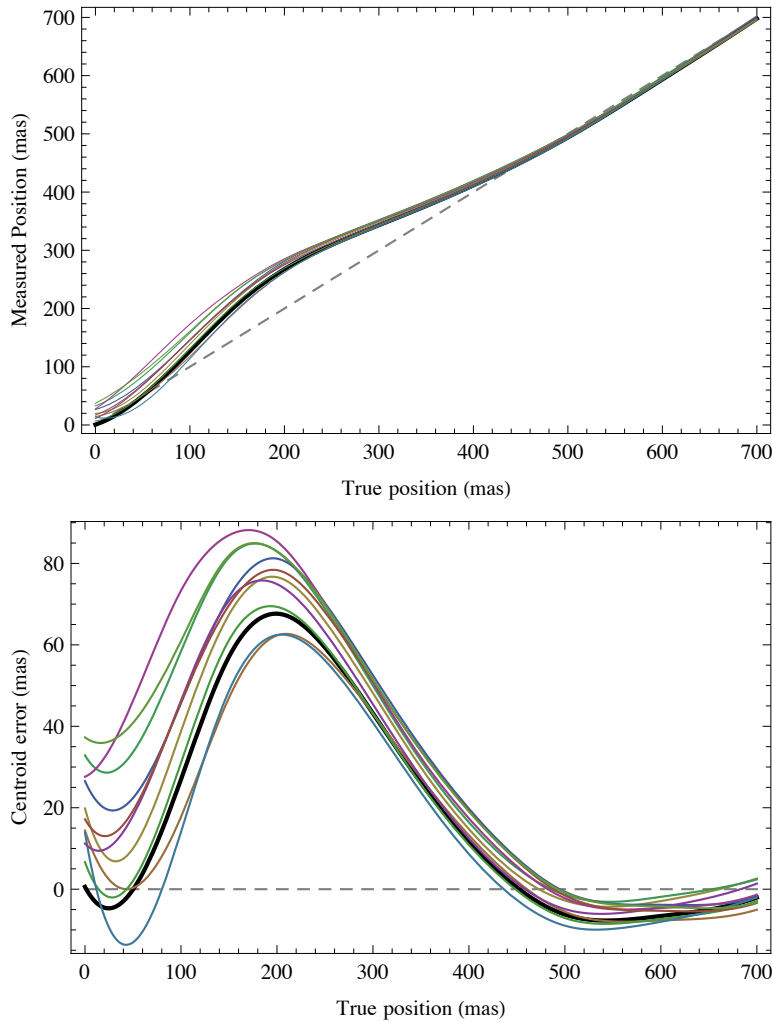
Figure 22: Simulations for the same effect, from Soummer 2011 draft technical report "Centroid Errors during Target Acquisition with MIRI Four Quadrant Phase Mask Coronagraphs". Note that the axis range displayed is different from the preceding figure, and the sign of the centroid error is reversed (due to showing here the quantity [measured-true] versus [true-measured] in Fig 21). Apart from these minor differences in data display, the results are consistent and support the same conclusions regarding MIRI coronagraphic target acquisition.

6.6 Comparison with TFI Science Team Published Results

Figure 23 shows a comparison of published models from the TFI team (model by Mathilde Beaulieu, published in Doyon et al. 2010) top, with WebbPSF simulations, bottom. The unocculted PSF profile is identical. For occulted PSFs, the profiles are similar but not identical: WebbPSF results in somewhat greater suppression than the TFI team's models at larger radii. This is believed to be due to a more detailed treatment in their models of effects such as pointing jitter and pupil misalignments. Because TFI

coronagraphy will not be pursued in the nTFI redesign, there is no need or reason to pursue any further work on the TFI coronagraphic model in WebbPSF.
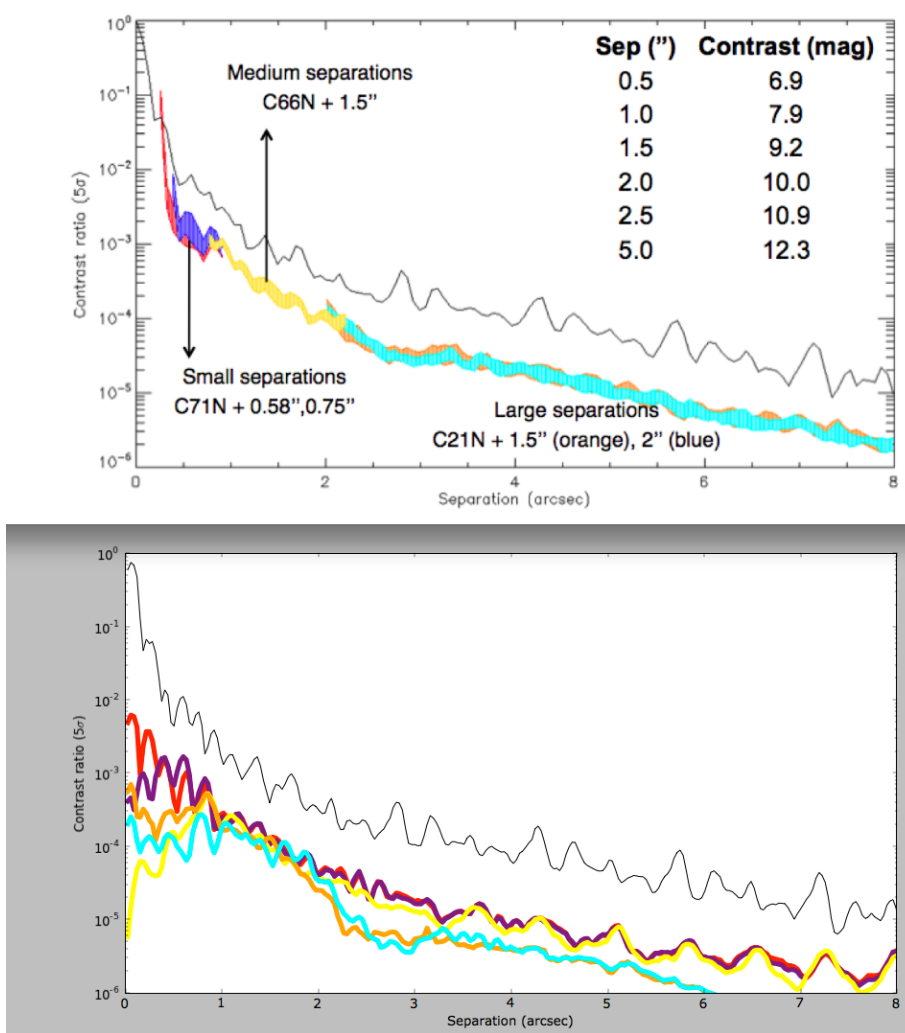

Figure 23: Comparison of TFI coronagraphy simulations. Top panel: results from Doyon et al. 2010. Bottom panel: Results from WebbPSF.

7.0 References

Anderson, Jay and King, Ivan. 2006, ACS Instrument Science Report 2006-01

Cox C. and Hodge, P. 2006 in "Space Telescopes and Instrumentation I: Optical, Infrared, and Millimeter", eds. J. C. Mather, H. A. MacEwen, & M. W. M. de Graauw, Proceedings of the SPIE, V. 6265, 62650W

Doyon et al. 2010. "The JWST Tunable Filter Imager", Proc SPIE, Vol. 7731.

Goodman, J. 1996. *Introduction to Fourier Optics, 2nd Edition*. McGraw-Hill Publishing. (or see *ibid., 3rd Edition*, 2005, Roberts & Company Publishers)

Krist, J. 1995, "Simulation of HST PSFs using Tiny Tim", Astronomical Data Analysis Software and Systems IV, ASP Conference Series, R.A. Shaw, H.E. Payne, and J.J.E. Hayes, eds. 77, 349.

Krist, John E., Beichman, Charles A., Trauger, John T., Rieke, Marcia J., Somerstein, Steve, Green, Joseph J., Horner, Scott D., Stansberry, John A., Shi, Fang, Meyer, Michael R., Stapelfeldt, Karl R., & Roellig, Thomas L. 2007, SPIE Conference Series 6693 16

Krist, John E., Balasubramanian, Kunjithapatham, Beichman, Charles A., Echternach, Pierre M., Green, Joseph J., Liewer, Kurt M., Muller, Richard E., Serabyn, Eugene, Shaklan, Stuart B., Trauger, John T., Wilson, Daniel W., Horner, Scott D., Mao, Yalan, Somerstein, Stephen F., Vasudevan, Gopal, Kelly, Douglas M., & Rieke, Marcia J. 2009, SPIE Conference Series, 7440 28

Krist, John E., Balasubramanian, Kunjithapatham, Muller, Richard E., Shaklan, Stuart B., Kelly, Douglas M., Wilson, Daniel W., Beichman, Charles A., Serabyn, Eugene, Mao, Yalan, Echternach, Pierre M., Trauger, John T., & Liewer, Kurt M. 2010, SPIE Conference Series , 7731 113

Hook, R. and Stoehr, F. 2008, "WFC3 Support in Tiny Tim", STSCI ISR WFC3 2008-014.

Makidon, Russell B., Lallo, Matthew D., Casertano, Stefano, Gilliland, Ronald L., Sirianni, Marco, & Krist, John E. 2006, SPIE Conference Series, 6270, 52

Makidon, R., Casertano, S., Cox, C. and van der Marel, R. "The JWST Point Spread Function: Calculation Methods and Expected Properties", 2007, JWST-STScI-001157, SM-12

Soummer et al. 2007 "Fast computation of Lyot-style coronagraph propagation." Optics Express vol. 15 pp. 15935

Soummer, R. 2010, "Inventory of JWST simulation software at STScI", JWST-STScI-002217

Check with the JWST SOCCER Database at: http://soccer.stsci.edu/DmsProdAgile/PLMServlet

To verify that this is the current version.